Earth Syst. Sci. Data, 16, 4777–4792, 2024
https://doi.org/10.5194/essd-16-4777-2024

Open Access Earth System Science Data

In situ airborne measurements of atmospheric parameters and airborne sea surface properties related to offshore wind parks in the German Bight during the project X-Wakes

Astrid Lampert, Rudolf Hankers, Thomas Feuerle, Thomas Rausch, Matthias Cremer, Maik Angermann, Mark Bitter, Jonas Füllgraf, Helmut Schulz, Ulf Bestmann, and Konrad B. Bärfuss

Institute of Flight Guidance, TU Braunschweig, Hermann-Blenk-Str. 27, 38108 Braunschweig, Germany

Correspondence: Astrid Lampert (astrid.lampert@tu-braunschweig.de)

Received: 14 February 2024 – Discussion started: 2 May 2024
Revised: 19 August 2024 – Accepted: 21 August 2024 – Published: 23 October 2024

Abstract. Between 14 March 2020 and 11 September 2021, meteorological measurement flights were conducted above the German Bight in the framework of the project X-Wakes. The scope of the measurements was to study the transition of the wind field and atmospheric stability from the coast to the sea, to study the interaction of wind park wakes, and to study the large-scale modification of the marine atmospheric boundary layer by the presence of wind parks. In total, 49 measurement flights were performed with the research aircraft Dornier 128 of the Technische Universität (TU) Braunschweig during different seasons and different stability conditions. Seven of the flights in the time period from 24 to 30 July 2021 were organised using a second research aircraft, the Cessna F406 of TU Braunschweig. The instrumentation of both aircraft consisted of a nose boom with sensors for measuring the wind vector, temperature and humidity and, additionally, a surface temperature sensor. The Dornier 128 was further equipped with a laser scanner for deriving sea state properties and two downward-looking cameras in the visible and infrared wavelength range. The Cessna F406 was additionally equipped with shortwave and longwave broadband radiation sensors for measuring upward and downward solar and terrestrial radiation. A detailed overview of the aircraft, sensors, data post-processing and flight patterns is provided here. Further, averaged profiles of atmospheric parameters illustrate the range of conditions. The potential use of the dataset has been already shown by the first few publications. The data of both aircraft are publicly available on the world data centre PANGAEA at https://doi.org/10.1594/PANGAEA.955382 (Rausch et al., 2023a).

1 Introduction

Renewable power from wind turbines already plays a major and increasing role in current and future worldwide energy supply (Veers et al., 2019). Despite the forecast of drastic declines in wind energy cost (Wiser et al., 2021), all phenomena significantly reducing the energy yield have to be carefully considered for the operation of current and the planning of future wind parks (Akhtar et al., 2021) and included in economic efficiency calculations (Lundquist et al., 2019). Due to spatial limitations and for sharing expensive infrastructure, offshore wind energy converters are mostly arranged as wind parks, containing up to 100 individual turbines, and as large clusters of the dimensions of tens of kilometres to 100 km, combining different wind parks. Ideas for using floating platforms or different foundation mechanisms at greater water depth have been developed (Manzano-Agugliaro et al., 2020), and wind measurements at first floating wind parks are currently investigated (Angelou et al., 2023).

Wind parks strongly interact with the atmosphere and induce changes to the wind resource (e.g. Akhtar et al., 2021). Wind park wakes reduce the wind speed and increase turbulence in downwind areas (Pettas et al., 2021; Syed et al., 2023). The wake recovery process can take several tens of

kilometres (Christiansen and Hasager, 2005; Li and Lehner, 2013), influencing downwind-located wind parks (e.g. Nygaard and Hansen, 2016; Cañadillas et al., 2020). However, this strongly depends on atmospheric conditions and, in particular, on the presence and altitude of a temperature inversion (Platis et al., 2020, 2022). Wakes of large wind parks reduce the available inflow wind speed and reduce the power output of subsequent downstream wind parks (El-Asha et al., 2017; Schneemann et al., 2020). Further, the vertical exchange is increased, which results in enhanced latent heat fluxes (Platis et al., 2023). The wake effects are superposed by spatial variability in the wind field, particularly for wind from land to sea with sudden changes in surface properties at the coastal transition (Djath et al., 2022).

As wind speed is one of the main drivers for sea state development, the reduced wind speed in wakes also results in modified wave spectra (Bärfuss et al., 2021), sediment transport (Rivier et al., 2016), ocean stratification and upwelling (Paskyabi, 2015), ocean circulation (Broström, 2008), and reduction in significant wave height (Ponce de León et al., 2011; Fischereit et al., 2022).

Therefore, it is of crucial importance to improve the knowledge about atmospheric processes and impacts related to wind energy extraction and dynamics on multiple scales, from individual turbine blades to large wind park clusters; to assess manipulation measures; and to train qualified personnel with interdisciplinary understanding for future decision-making and site selection (Spyridonidou and Vagiona, 2020).

Airborne measurements can be used as flexible tools for directly measuring the offshore wind field and surface properties and modifications induced by wind parks on large scales (Platis et al., 2018). In the framework of the project WIPAFF (WInd PArk Far Field; Platis et al., 2020), an extensive airborne dataset has been acquired to demonstrate the existence and extent of wind park wakes under stable conditions (Bärfuss et al., 2019; Lampert et al., 2020). Since the acquisition of this first comprehensive dataset in 2016/2017, new wind park clusters have been built in the German sector of the North Sea. Therefore, the project X-Wakes acquired additional airborne datasets in 2020/2021 with the aim to investigate the following phenomena:

- interaction of wakes of different wind parks
- large-scale effects of wakes on downstream wind parks
- global blockage effect modifying the flow field upstream of wind parks
- coastal transition of wind field and stability.

One key challenge of interpreting airborne measurements is the fact that the wind field is both temporally and spatially variable, and the assumption of steady conditions is not valid for distances of 100 km and timescales of several hours. Therefore, two aircraft were deployed simultaneously for several cases, one measuring the flow field upstream of a wind park or wind park cluster and the other measuring the downstream flow field. The same was done for studying the coastal effect with two aircraft.

The aim of this article is to provide an introduction to the airborne measurements published in Rausch et al. (2023a). The structure is as following: Sect. 2 presents the two aircraft of TU Braunschweig used for the measurement flights. Section 3 shows the instrumentation of the two aircraft. Section 4 explains the different flight patterns applied to study the phenomena mentioned above, and references to detailed studies already performed with the dataset. Section 5 illustrates the atmospheric conditions during the measurement flights. Section 6 presents exemplary measurements of wind park wakes, blockage effect, coastal effect, the wind field modifications above wind parks, radiation measurements for cloud identification, and small-scale changes in sea surface. Finally, Sect. 8 provides a conclusion.

2 Research aircraft

Two research aircraft were used for the investigation of wind park wakes and modifications of the atmospheric boundary layer in the vicinity of offshore wind parks during the process of replacing the measurement aircraft Dornier 128 of TU Braunschweig by the successor aircraft Cessna F406 (Fig. 1). In 2021, the last meteorological measurements campaigns of the Dornier 128 and the first campaigns of the Cessna F406 were performed in parallel.

2.1 Dornier 128

The Dornier 128 with the call sign D-IBUF (Do128-6) is a twin-engine propeller aircraft which had been deployed by TU Braunschweig for atmospheric research from 1986 until 2021. It was operated at an air speed of 60–65 $\mathrm{m\,s^{-1}}$. The aircraft is described in detail in Corsmeier et al. (2001). An overview of meteorological measurement campaigns with this research aircraft is given in Lampert et al. (2020).

2.2 Cessna F406

The Cessna F406 with the call sign D-ILAB is a twin-engine propeller aircraft which has been chosen as the successor for the successful aircraft Dornier 128. It has similar specific properties which are required for operation in the atmospheric boundary layer. The non-pressurised cabin allows for the installation of equipment in the fuselage looking through openings in the roof and on the bottom. It can fly at a low cruising speed of 70 $\mathrm{m\,s^{-1}}$ for high-resolution measurements. The two engines enable operations at low altitudes as required for the flights at hub height above the North Sea. The aircraft provides space for two pilots and two to three operators depending on the installed measurement equipment in the cabin.

Figure 1. The research aircraft Dornier 128 D-IBUF (left) and Cessna F406 D-ILAB (right) with striking colours for good visibility and the characteristic nose boom for meteorological measurements flying above their home base, the Braunschweig airport. Photo by Florian Szczepanek, https://www.aviation-media.com/ (last access: 15 October 2024).

The state of the art data acquisition system consists of a core computer with several interfaces (such as different digital and analogue input and output signals, including the format ARINC429, and serial and ethernet ports). This computer receives the sensor data in real time, provides time stamps to the data packages and stores the raw data items on an internal hard drive. It provides the raw data via ethernet to a second computer, which makes real-time calculations for, for example, wind speed in all three dimensions. The second computer performs unit conversions and applies calibration and correction factors where required. At the time of the campaign, it provided a text-based user interface with tables and columns for several raw and calculated parameters. Now it also includes a graphical user interface with maps, primary flight display, system surveillance and protocol. The pre-selected parameters are recorded on a removable hard drive which allows for quick data transfers after a measurement flight. The raw data on the first computer remain in the aircraft as backup and are overwritten after a couple of flights. This approach ensures reliable data handling and data security. A third computer is used to provide online graphics and quicklooks of different parameters since the beginning of the recording. This feature displays time series and vertical profiles and can be used for on-board decision-making, for example, to determine the most relevant flight altitude for a specific mission. The overall layout of the data acquisition and recording system allows for a flexible integration of additional sensors for synchronous recording. The user interface for monitoring of the flight and mission parameters as well as an interaction with the system is installed on two different mission consoles. In addition, a wireless access point is implemented to stream the real-time data inside the cabin, which allows more scientists or observers to monitor the acquired parameters on a mobile device as well.

Figure 2 shows a front view of the aircraft with the nose boom. Another sensor below the aircraft nose next to the nose boom is a forward-looking camera. The location of the measurement head in front of the aircraft is a compromise between structural requirements of the aircraft frame and distance in front of the aircraft to perform measurements in the undisturbed airflow. The vibrations of the measurement head were measured during the initial flight tests and found to be negligible. So, a correction is not required.

The data acquisition system can record so-called “events”, i.e. specific points in time when one of the cockpit crew members or one of the scientists/observers has detected a noticeable event during the flight and triggered the “event button”. Such an event increases an internal counter and writes a short protocol note into the logfile, complemented by a photo of the forward-looking camera. This feature is very useful during the process of data evaluation.

3 Sensors and data processing

The instrumentation and data processing of the Dornier 128 have been described in detail in Lampert et al. (2020). There-

Figure 2. The research aircraft Cessna F406 D-ILAB. Photo by Thomas Feuerle.

fore, the instrumentation of the Dornier 128 is only shortly summarised. The instrumentation of the Cessna F406 is presented in more detail, in particular if it is different from the sensors on board the Dornier 128. The temperature, pressure and humidity sensors were calibrated before and after each campaign. The temperature sensors are calibrated using a high-precision resistance decade. All static pressure and differential pressure sensors are calibrated over the respective specified pressure range using two Weston Aerospace DPM7885 absolute pressure transducers as reference. For calibrating the Vaisala Humicap humidity sensor, the sensor head is inserted into a salt chamber containing one of four different saturated salt solutions. The reading given by the probe or transmitter is then adjusted to the humidity value that the specific salt solution generates at that particular temperature. The calibrations described above were carried out on 9 March 2020, 26 March 2021 and 19 June 2021.

The altitude refers to height above mean sea level (WGS84 data from the Global Navigation Satellite System, GNSS, without geoid height), and the radar altitude provides the height above the surface.

3.1 Temperature

The concept of using two complementary sensors for temperature has been implemented for both aircraft. In the data processing, the data from a highly accurate temperature sensor, 102DB1AG (Rosemount, USA), and a fast temperature sensor, 102E4AL (Rosemount, USA), can be combined or used for quality check. Further, the effect of self-heating induced by the air speed is taken into account in the data processing (Stickney et al., 1994; Bärfuss et al., 2018). The method of calculating the best possible result based on a slow but more accurate and a fast but drifting sensor is done by complementary filtering, as described in detail in Bärfuss et al. (2018).

3.2 Humidity

Humidity is measured with three sensors based on different measurement principles: in the nose boom of the Dornier 128, there is a TP 3-S dew point mirror (Meteolabor, Switzerland), a Humicap H233 capacitive sensor (Vaisala, Finland) and an L-6/HMS-2 Lyman-alpha sensor (Buck Research, USA). The dew point mirror provides the most precise measurements at a temporal resolution of 1 Hz. The Lyman-alpha, based on optical absorption in the ultraviolet wavelength range, delivers data at a high temporal resolution of 100 Hz but with a drifting signal.

In the nose boom of the Cessna F406, there are a dew point mirror and capacitive sensor of the same type and a KH-20 optical sensor (Campbell Scientific, USA) based on absorption in the ultraviolet wavelength range for fast water vapour fluctuations.

3.3 Wind vector and pressure

Determining the wind vector is based on the principle of subtracting the air speed vector from the ground speed vector for both aircraft. The ground speed vector is derived from the high-precision measurements of the aircraft position and attitude using an integrated system of inertial measurement unit (IMU) and Global Navigation Satellite System (GNSS). For the air speed vector, measuring the airflow angles, the angle of attack (angle between the velocity vector of the aircraft relative to the air and the aircraft longitudinal axis, describing the longitudinal component of the aircraft velocity) and the angle of sideslip (angle between the velocity vector and the projection of the aircraft longitudinal axis, which describes whether there is a lateral component to the aircraft velocity) are required. This is done via a five-hole probe at the front of the nose boom and needs fusing the data with high-precision attitude data (Lenschow, 1972). The static and dynamic pressure as well as the pressure differences occurring at the five-hole probe (Rosemount, USA) are measured with

pressure transducers of Setra, USA. The pressure transducers are located right behind the probe to minimise the length of the required tubes. While on-board the Dornier 128 the inertial data is measured with the IMU iNAV-RQH-1003 (iMAR, Germany) and the GNSS data with an external GNSS receiver OEM6 (NovAtel, Canada), on-board the Cessna F406, the GNSS receiver OEM6 (NovAtel, Canada) is already integrated into the successor IMU iNAT-RQT-4001 (iMAR, Germany). Accuracy and resolution of the systems used are compared in Table 1. The accuracy of the horizontal wind speed components of the D-IBUF is better than 0.5 m s^{-1} and of the vertical wind speed component better than 0.1 m s^{-1} (Corsmeier et al., 2001). As pressure measurements are the bottleneck for wind measurement accuracy, and the D-ILAB deploys the same pressure sensor types as the D-IBUF, no differences in wind speed accuracy between the two aircraft is expected, which was also the observation during calibration flights.

3.4 Surface temperature

The surface temperature of both aircraft is measured with an infrared radiation thermometer (KT15.82D in the Dornier 128 and KT19.85 in the Cessna F406, both by former Heimann, now Heitronics, Germany), with an accuracy of ±1.2 K at 20 °C surface temperature and a temporal resolution of 20 Hz. As the infrared radiation passes through the atmosphere between the surface and the aircraft, with an unknown concentration of humidity, particles or other factors that potentially influence the infrared radiation, the measured surface temperature depends on the flight altitude with a linear factor of typically between 0.1 and 0.15 K per 100 m.

3.5 Sea surface deflection

The VZ-1000 laser scanner (Riegl, Austria) is included on board the Dornier 128 to measure sea state properties through an opening in the fuselage. With this setup, it is possible to measure the significant wave height (Bärfuss et al., 2020) and derive wave spectra (Bärfuss et al., 2021) along the flight path. The laser scanner covers a line of sight range of up to 450 m.

During these flights, no laser scanner was available on board the Cessna F406.

3.6 Cameras

In the Dornier 128, two downward-looking cameras are integrated: the MV1-D1312-G2 (Photonfocus, Switzerland) for the visible wavelength range and the A35SC (FLIR, Germany) for the infrared wavelength range. In the Cessna F406, nadir-looking cameras had not yet been installed.

3.7 Radiation

Only in the Cessna F406, sensors for measuring broadband upward and downward solar and terrestrial irradiance are included: two CMP22 pyranometers (Kipp and Zonen, The Netherlands) for measuring solar irradiance in the wavelength range 210–3600 nm and two CGR4 pyrgeometers (Kipp and Zonen, The Netherlands) for measuring terrestrial irradiance in the wavelength range 4.5–42 µm. The sensors' response time is given as < 1.7 s for the solar radiation and < 18 s for the terrestrial radiation, which is quite low for the high ground speed of the aircraft and cloud structures typically varying on the scale from a few hundred metres to 1 km for shallow convective clouds (Fast et al., 2019). Radiation measurements have been included to complement the atmospheric measurements and as an indicator to identify cloudiness.

4 Flight planning and flight patterns

Generally, the flights aimed to provide direct in situ information on modifications of the wind field and the structure of the atmospheric boundary layer related to offshore wind energy. In particular, the interaction of wakes of different neighbouring wind parks and wind park clusters was investigated in order to understand processes, validate simulations and enable realistic forecasts of wake effects for future wind park scenarios.

An overview of all trajectories flown during the 49 X-Wakes flights in the German Bight is provided in Fig. 3. Also, the names of the wind park clusters N2, N3 and N4 are indicated there. As a first orientation, the approximate wind direction and wind speed at hub height are provided, which are highly variable in time, in horizontal direction and with altitude. The flexible flight permission with low-level flights down to 50 ft (around 15 m) was valid for the German airspace. The flights were mostly performed from the Wilhelmshaven airport with the ICAO (International Civil Aviation Organisation) code EDWI. When no overnight stays were possible due to pandemic travel restrictions, the measurement flights were done directly from the home base, the airport Braunschweig with ICAO code EDVE. An overview of all flights, dates, times, prevailing wind speed and wind direction, wind parks, flight patterns, cloud conditions, and simultaneous satellite overpasses is provided in Tables 2 and 3.

4.1 Meander at hub height (meander)

To investigate the interaction between several wind parks or even wind park clusters and quantify wake effects, the flight pattern "meander" was applied (Fig. 4a). The wind speed reduction in wakes can be on the order of up to 30 % (Cañadillas et al., 2020). Transects perpendicular to the mean wind direction were flown across the interacting wind park wakes. The distance between the legs was adapted to the atmo-

Table 1. Technical data of the inertial measurement units iNAV-RQH-1003 (Dornier 128) and iNAT-RQT-4001 (Cessna F406).

Aircraft		Dornier 128 D-IBUF	Cessna F406 D-ILAB
Inertial navigation system		iNAV-RQH-1003	iNAT-RQT-4001
Gyroscopes	Range	$\pm 400^\circ\,s^{-1}$	$\pm 395^\circ\,s^{-1}$
	Bias stability	$0.002^\circ\,h^{-1}$	$< 0.001^\circ\,h^{-1}$
	Resolution	0.0003°	0.00033°
	Scale error	< 5 ppm	< 15 ppm
	Linearity error	< 5 ppm	< 10 ppm
Accelerometers	Range	± 20 g	± 20 g
	Bias stability	$< 10\,\mu g$	$< 12\,\mu g$
	Resolution	$< 5\,\mu g$	$< 5\,\mu g$
	Scale error	< 100 ppm	< 100 ppm
	Linearity error	$< 20\ \mu g\,g^{-2}$	$< 30\ \mu g\,g^{-2}$
Data rate		300 Hz	400 Hz
True heading		$< 0.04^\circ\,s^{-1}$ (lat)	$< 0.028^\circ\,s^{-1}$ (lat) free inertial $< 0.01^\circ$ with GNSS
Attitude accuracy		$< 0.01^\circ$	$< 0.025^\circ$ free inertial $< 0.01^\circ$ with GNSS
Position accuracy		< 0.8 nm h^{-1}	< 0.8 nm h^{-1} free inertial < 1.6 m with GNSS
GNSS receiver		NovAtel OEM6 (external)	NovAtel OEM6 (internal)

Table 2. Overview of the X-Wakes measurements for Flights 1–25 with the research aircraft Dornier 128. The flight patterns are meander (M), blocking (B) coast (C) or above (A) as indicated in Sect. 4. One short flight was dedicated to comparing sea surface measurements to buoy measurements. The following abbreviations are used for clouds: Cu (cumulus), hum (humilis), Sc (stratocumulus), St (stratus), Ac (altostratus), Ci (cirrus), Cs (cirrostratus), and r.s. (rain showers). The overpass times of the satellites Sentinel-1A (S1A) and Sentinel-1B (S1B) are provided as well.

Flight no.	Date	Time [UTC]	Wind park cluster	Pattern	Altitude [m]	Wind speed [m s^{-1}]	Wind direction [°]	Cloud	Satellite [UTC]
1	14 Mar 2020	11:55–15:43	N3	B	120	11	150	3/8 Ac, Ci	S1B, 17:17
2	15 Mar 2020	10:01–13:49	N3	C	120	14	190	7/8 Sc	S1A, 17:02
3	17 Mar 2020	08:42–12:33	N4	B	90	12	240	n.a.	S1A, 05:35
4	21 Mar 2020	09:54–14:06	N4	C	90	11	90	1/8 Cu hum	S1B, 17:10
5	21 Apr 2020	07:58–11:27	N4	C	90	12	90	clear sky	S1B, 05:43
6	21 Apr 2020	12:08–15:54	N4	C	90	17	90	clear sky	–
7	24 Apr 2020	07:29–07:31	N4	Buoy		8	330	Sc	S1B, 17:16
8	05 May 2020	07:32–11:28	N4	B	90	8	350	5/8 Cu	–
9	05 May 2020	12:08–16:02	N4	B	90	7	340	clear sky	–
10	08 May 2020	07:29–11:33	N4	B	90, 120	7	240	7/8 Ci	S1B, 05:52
11	08 May 2020	12:04–16:05	N4	B	90, 120	9	240	7/8 Ci	S1B, 17:04
12	29 Jun 2020	12:58–17:04	N2, N3, N4	M	120	15	230	7/8 Sc, r.s.	S1A, 17:19
13	30 Jun 2020	07:48–11:38	N4	B	90	17	250	7/8 Sc, r.s.	–
14	30 Jun 2020	12:28–16:26	N4	B	90	17	260	5/8 Sc, Ac, Ci, r.s.	S1B, 17:08
15	01 Jul 2020	10:36–14:43	N3	C	120	10	180	6/8 Cu, r.s.	S1A, 05:52
16	02 Jul 2020	10:54–14:04	N4	B	90	3	310	6/8 Sc, Ci, r.s.	S1B, 05:43
17	03 Jul 2020	09:43–13:44	N2, N3, N4	M	120	10	240	8/8 Sc, r.s.	S1A, 05:35
18	13 Jul 2020	13:12–17:24	N4	B	90	6	220	3/8 Ac, 7/8 Cs	S1A, 17:02
19	14 Jul 2020	12:26–16:05	N2, N3	M	120	7	270	2/8 Cu hum, 7/8 Sc, r.s.	S1B, 05:43
20	15 Jul 2020	07:42–11:42	N4	B	90	5	320	2/8 Cu, 6/8 Ac	S1A, 05:35
21	15 Jul 2020	12:15–16:01	N4	B	90	5	300	2/8 Cu, 4/8 Ac	–
22	23 Jul 2020	06:58–11:00	N3	C	120	8	190	8/8 St, r.s.	–
23	23 Jul 2020	11:28–15:30	N2, N3, N4	M	120	10	225	5/8 Sc, r.s.	S1A, 17:25
24	24 Jul 2020	07:01–11:15	N2, N3	M	120	10	270	2/8 Cu	S1B, 17:16
25	27 Jul 2020	09:23–13:30	N3	C	90–240	10	180	8/8 As	S1A, 05:40

Table 3. Overview of the X-Wakes measurements for Flights 26–49 with the research aircraft Dornier 128. The flight patterns are meander (M), blocking (B) coast (C) or above (A) as indicated in Sect. 4. During one short flight, only profile measurements were obtained. The 7 flights with two aircraft in parallel were conducted between 24 July 2021 and 30 July 2021 (numbers printed in bold letters). The same symbols and abbreviations are used as in Table 2.

Flight no.	Date	Time [UTC]	Wind park cluster	Pattern	Altitude [m]	Wind speed [m s^{-1}]	Wind direction [°]	Cloud	Satellite [UTC]
26	28 Jul 2020	06:52–10:50	N2, N3	M	120	13	250	3/8 Cu, r.s.	–
27	28 Jul 2020	11:20–15:15	N4	B	90	13	250	2/8 Cu, 4/8 Ac	–
28	23 Sep 2020	05:15–09:18	N3	C	120	12	220	5/8 Sc	S1A, 05:55
29	23 Sep 2020	10:59–15:03	N3	C	120	10	210	2/8 Sc, 7/8 Ac	S1A, 17:08
30	24 Sep 2020	07:07–10:56	N2, N3, N4	M	120	17	230	2/8 Cu	S1B, 05:48
31	24 Sep 2020	11:56–12:46		Profiles		10	210	2/8 Cu	–
32	24 Sep 2020	13:21–16:35	N3	C	120	13	190	7/8 Sc, r.s.	–
33	25 Sep 2020	09:45–13:54	N3	C	120	10	180	3/8 Cu, Cs	S1A, 05:40
34	08 Apr 2021	07:51–11:53	N4	B	90	11	260	7/8 Sc, r.s.	–
35	08 Apr 2021	12:21–16:30	N2, N3, N4	M	120	15	240	7/8 Sc	S1A, 17:16
36	12 Apr 2021	07:32–11:36	N4	B	90	8	260	3/8 Cu, r.s.	–
37	12 Apr 2021	12:03–16:03	N4	B	90	9	260	4/8 Cu, r.s.	–
38	13 Apr 2021	07:30–11:30	N3	M	120	11	300	5/8 Cu, r.s.	–
39	13 Apr 2021	12:02–16:02	N3	M	120	10	300	5/8 Cu, r.s.	S1A, 17:24
40	14 Apr 2021	07:30–11:25	N3	M, B	120	7	330	2/8 Cu, 3/8 Cs, r.s.	–
41	14 Apr 2021	11:53–15:55	N3	M, B	120	6	330	3/8 Cu, r.s.	S1B, 17:16
42	24 Jul 2021	07:46–12:03	N4	C	90	7	90	7/8 Cs	–
43	24 Jul 2021	12:40–16:05	N4	C	90	7	70	7/8 Cs	S1B, 17:24
44	27 Jul 2021	10:09–14:24	N2, N3, N4	A, M	120	10	240	4/8 Cu, Ac, Ci	S1A, 05:48
45	28 Jul 2021	08:34–13:00	N3	C	120	10	200	3/8 Cu, Ci, r.s.	S1B, 05:41
46	29 Jul 2021	08:36–10:57	N2, N3	A, M	120	17	240	8/8 Sc, r.s.	–
47	29 Jul 2021	12:40–17:02	N2, N3, N4	A, M	120	17	245	3/8 Cu, r.s.	–
48	30 Jul 2021	07:37–12:07	N2, N3, N4	A, M	120	10	240	3/8 Cu	S1A, 17:24
49	11 Sep 2021	12:51–17:13	N3, N4	M	120	9	240	8/8 St, r.s.	S1A, 17:17

spheric stability, as very long wakes occur mostly for stable conditions (Cañadillas et al., 2020). For stable conditions, the spacing between legs was typically 10 km. If possible, flight legs were performed at hub height upstream, between wind parks and downstream. A safety distance of 500 m was kept to the closest row of wind turbines.

Further, vertical profiles were performed at different locations and times from an altitude of 15 m up to 1 km, if permitted by clouds, to document atmospheric stability and wind shear. In this case, the aircraft climbed continuously with a typical vertical speed of 5 m s^{-1}, and descended again, with the same vertical speed, corresponding to a horizontal translation of around 12 km per profile.

For the occasions of two aircraft, the second aircraft performed flight legs upstream of the wind park clusters or above the wind parks. The meander flight pattern was deployed during 17 out of the 49 flights. Results using the meander flight patterns have been published in Cañadillas et al. (2022) and zum Berge et al. (2024).

4.2 Blockage effect (blocking)

The erection of large wind park clusters provides an obstacle for the flow, with the consequence that the air tends to flow partly around and above the wind parks instead of passing straight through the wind turbines. This so-called blockage effect was investigated with a particular pattern ("blocking") upstream of the wind park clusters. The expected order of magnitude of the effect is much lower than the wake effects and in the range of up to 4 % (Schneemann et al., 2021).

To investigate the flow deflection around wind parks, flights were performed directly upstream of wind parks (Fig. 4b). The flight permission allowed us to approach a minimum distance of 500 m to the closest wind turbines. As the effect is expected to only be small, in the range of few percent, flights were performed as close to the wind parks as possible, with upstream distances between 500 m and 2 km and distances between legs from 100 to 500 m. The blocking flight pattern was deployed during 16 out of the 49 flights. An example of the measurements of the blocking effect is shown in Sect. 6. As the effect is very small, it is difficult to distinguish it from the spatial and temporal variability, and so far no results using the blocking flight patterns have been published.

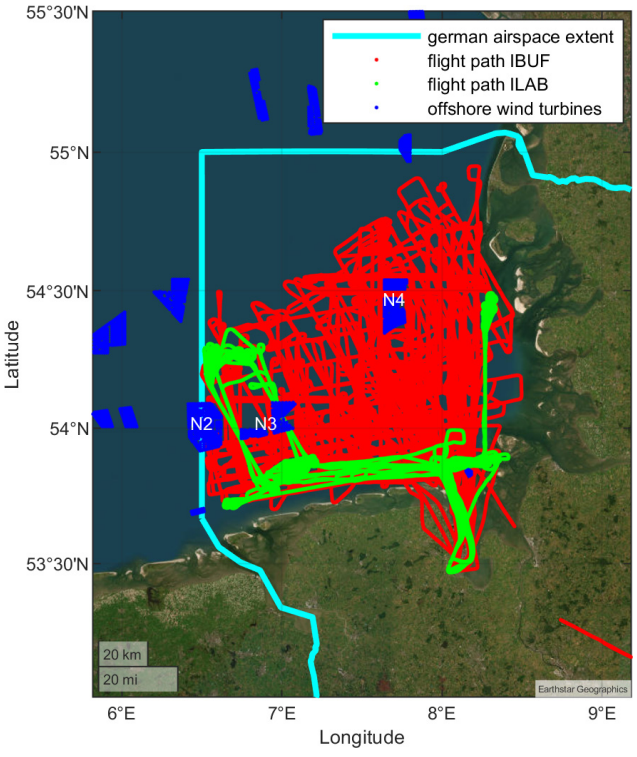

Figure 3. Overview of the airborne measurements conducted in the framework of the project X-Wakes. The light-blue line indicates the borders of the German airspace for which the flight permission was valid. Wind turbines in operation on the last flight day, 11 September 2021, are displayed in dark blue. All the flight tracks of the Dornier 128 are shown in red, and the flight tracks of the Cessna F406 in green. The names of the wind park clusters N2, N3 and N4 are indicated in white letters,

4.3 Coastal effect (coast)

The phenomenon of the coastal transition was another target of the measurement flights. The coastal effect means that the abrupt changes in the surface properties at the coast, with lower surface roughness and different heat capacity, lead to modifications of the wind field and thermal stratification (Schulz-Stellenfleth et al., 2022), which is particularly challenging to include in simulations (Siedersleben et al., 2018b). The increase or decrease in wind speed due to synoptic-scale changes and coastal effect can be on the order of several metres per second (e.g. Platis et al., 2018; Djath et al., 2022).

To investigate changes induced by coastal effects on spatial scales of 50 km, the flight pattern "coast" was applied, which consists of meander patterns along the coastline and perpendicular to the prevailing wind direction at hub height (which is 90 m for the N4 cluster close to the eastern coast of the German Bight and 120 m for the N2 and N3 clusters close to the southern coast of the German Bight). Additionally, offshore vertical profiles were performed at the beginning and end of each leg to document the changes in stability. For the combined flights with two aircraft (flight 42 to flight 48), the Cessna F406 repeated the same legs closest to the coast and the Dornier 128 performed meander flight legs from the coast to the open water to be able to separate the effects of temporal changes in the inflow conditions and spatial effects induced by the coast.

The "coast" flight pattern was deployed during 14 out of the 49 flights.

Results using the coast flight patterns have been published in Schulz-Stellenfleth et al. (2022) and Cañadillas et al. (2023).

4.4 Above wind park (above)

Finally, flights were not only performed upstream or downstream of the wind parks, but also above the wind parks to investigate changes in the boundary layer. This was done with the flight pattern "above" (Sect. 4.4).

For the flights with two aircraft dedicated to investigating wakes, the Dornier 128 performed the meander pattern downstream of the wind parks, while the Cessna F406 sampled upwind conditions and performed additional flight legs above the wind parks to investigate the effect above rotor height. The flights above the wind parks were done at an altitude of 75 m above the top of the rotor blades, which corresponds to an altitude of 255 m. Flight legs above wind parks were conducted with the Cessna F406 during four out of the seven joint measurement flights. So far, no results using the above flight pattern have been published.

5 Atmospheric conditions

To get an overview of the atmospheric conditions during the measurement flights, the following sections illustrate the vertical profiles with the median values, the 25 % and 75 % percentile, and a histogram to indicate the occurrence of the values during the flights. The measurements are not representative of a climatology as they were conducted during different seasons, mainly in spring and summer, and under visual flight conditions (cloud base height above 400 m for broken or overcast cloud cover and visibility exceeding 5 km). In the illustrations, each sample in the histograms originating from raw 100 Hz was filtered and downsampled to a rate of 7.5 Hz. Additionally, the lapse rate was median-filtered, with a width of 1 s.

5.1 Temperature

As the flights were performed during different seasons (earliest flight of the year on 14 March and the last flight on 25 September), the temperature is highly variable between the flights. The temperature near the surface was between 4 and 19 °C (see Fig. 6). Generally, temperature decreased with altitude. A slight temperature inversion up to an altitude of 50 m is visible in the mean profile, and, on average, there is a temperature inversion at an altitude of around 850 m. The

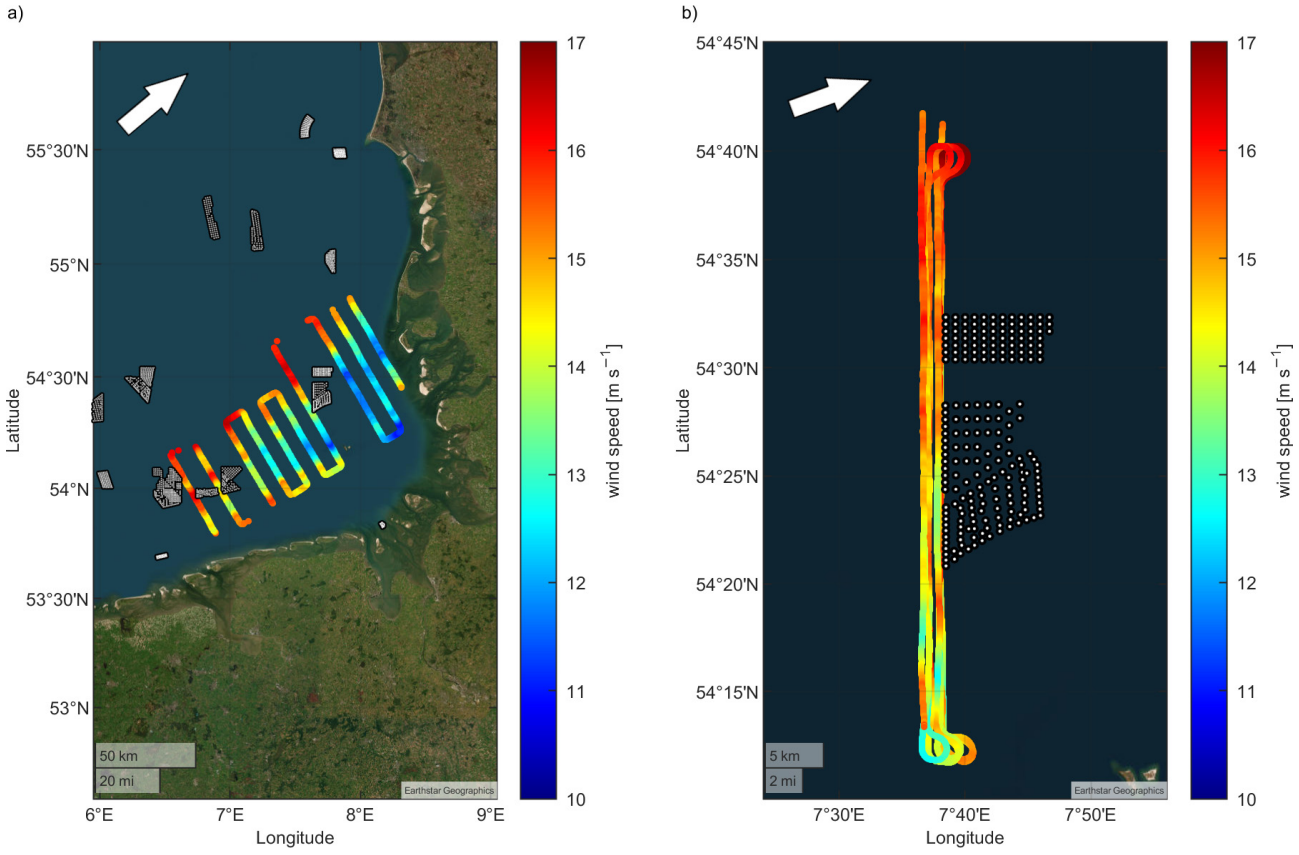

Figure 4. **(a)** Example of the meander pattern during flight 12 on 29 June 2020. The prevailing wind direction was from 230°. **(b)** Example of the blocking pattern during flight 13 on 30 June 2020. The prevailing wind direction was from 250°. The main pattern was flown at hub height, and only data measured at hub height are included in the figures.

whole flights were taken into account; therefore, temperature values during takeoff and landing are included, which may differ significantly from temperature values above the North Sea. The grey scale illustrates that the flights were performed as blocks, and not distributed continuously over time: lower temperatures, with near-surface air temperature in the range from 4 to 5 °C, occurred during the frequent measurements in early spring (March and April), but most flights were performed during the summer season with relatively warm near-surface air temperature in the range of 15 to 19 °C (see Tables 2 and 3). Therefore, the atmospheric conditions during the flights do not represent climatologically relevant statistics.

5.2 Stability

Figure 7 shows the distribution of the lapse rate as an indicator of stability for all flights. Values near zero indicate neutral conditions. Most measurements were performed for neutral and slightly stable conditions. For wake measurements and coastal effect, stable conditions were selected on purpose for the measurement flights, as the strongest effects are associated with stable conditions. For investigating the blockage effect, both stable and unstable stratification were probed. During spring and summer, wind directions from land are typically associated with warmer air masses during the day than the sea surface, leading to stable stratification. X-Wakes investigated not only the extreme cases of stability, but also the interaction of wind park wakes for different stability regimes.

What is notable is the enhanced stability at the altitude of the lowest 100 m. On average, there is a strong increase in stability within the lowermost 100 m. This is associated with the altitude of the temperature inversion (see Fig. 6) and has important consequences for the development of the wake and if there is a warming or cooling effect downstream of the wind park (Siedersleben et al., 2018a).

5.3 Wind speed

Figure 8 shows an overview of the wind speed conditions encountered during the measurement flights. The flights were performed under different wind speed conditions. At hub height, the wind speed varied between around 3 and 17 m s^{-1}, but most measurements were performed in the wind speed range between the cut-in speed of 4 m s^{-1}, where the wind turbines start turning, and the rated wind speed

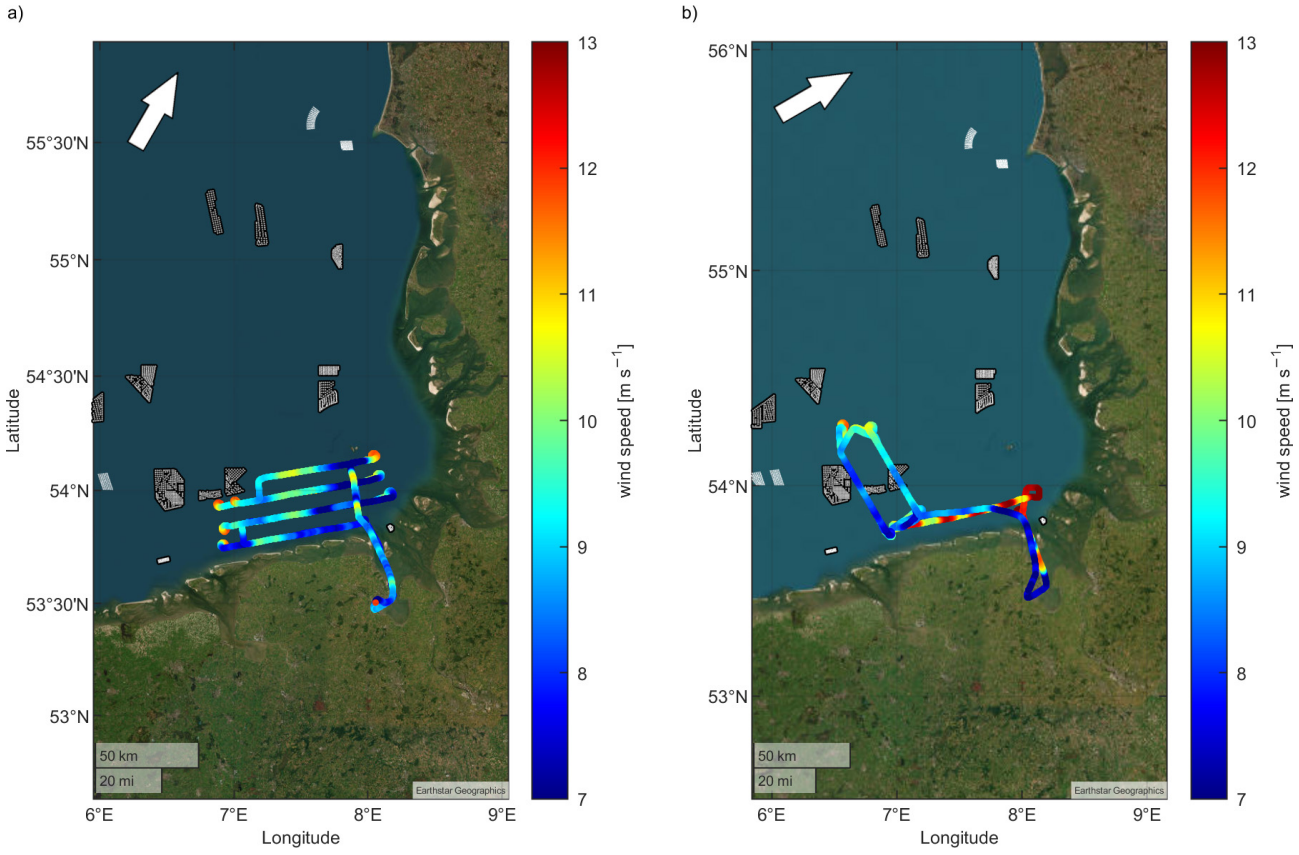

Figure 5. **(a)** Example of the coast pattern during Flight 29 on 23 September 2020. The prevailing wind direction was from 210°. **(b)** Example of the above pattern during Flight 48 on 30 July 2021. The prevailing wind direction was from 240°. The turns were used to perform vertical profiles, which means that the wind speed was generally higher than during flight legs at constant altitude. In contrast to Fig. 4, data of the whole flight are included and not only the data obtained at hub height.

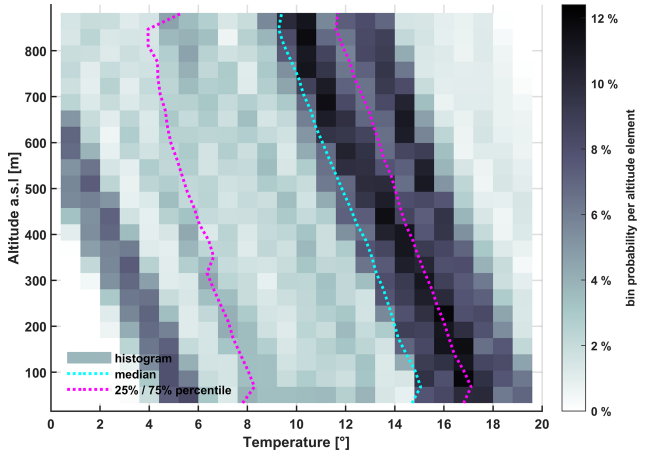

Figure 6. Temperature encountered during all measurement flights. The light-blue line represents the median of all profiles, the magenta lines indicate the percentiles including 25 % and 75 % of all values, and the grey scale is a histogram showing the frequency of the occurrence of the temperature values.

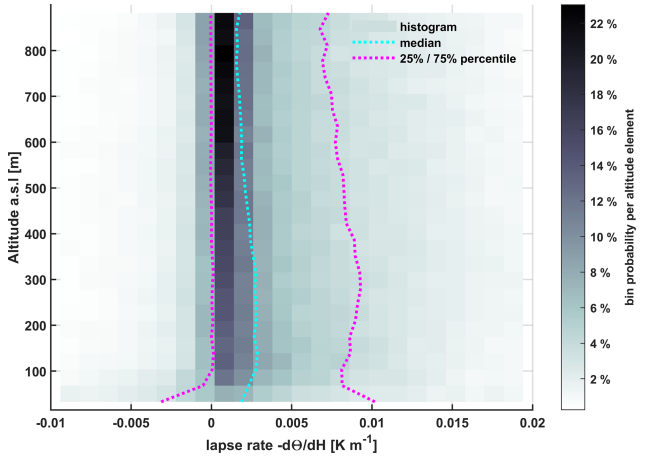

Figure 7. Lapse rate as an indicator of atmospheric stability. The light-blue line represents the median of all profiles, the magenta lines indicate the percentiles including 25 % and 75 % of all values, and the grey scale is a histogram showing the probability of the occurrence of the lapse rate values.

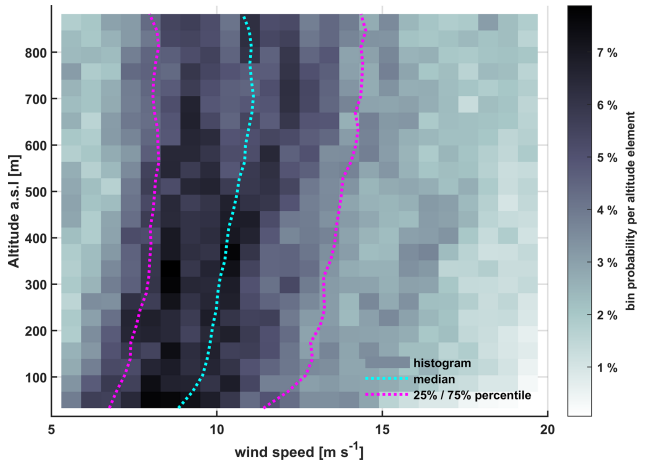

Figure 8. Wind speed conditions during all measurement flights. The light-blue line represents the median of all profiles, the magenta lines indicate the percentiles including 25 % and 75 % of all values, and the grey scale is a histogram showing the probability of the occurrence of the wind speed values.

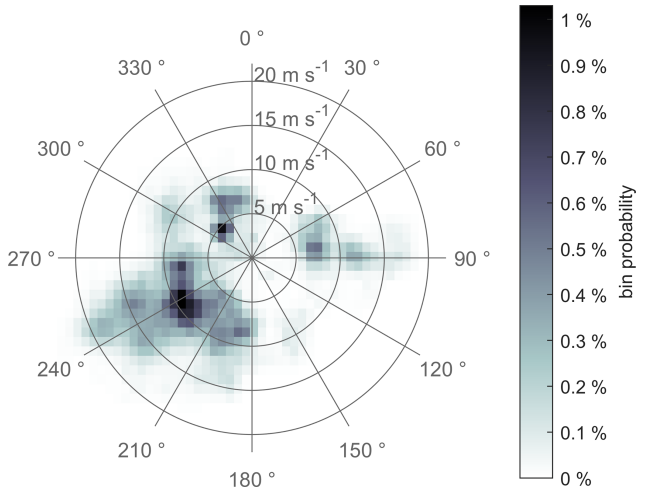

Figure 9. Wind rose of the conditions encountered during all measurement flights. The grey scale is a histogram showing the probability of the occurrence of the wind speed values in combination with wind direction.

of 12 m s^{-1}, where the wind turbines reach their maximum power output. In this wind speed range, the power output cubically depends on the wind speed; therefore, reductions in wind speed have a direct impact on the energy yield.

5.4 Wind direction

Figure 9 shows a wind rose diagram of the wind speed and wind direction that was observed during all measurement flights. The measurement flights covered average wind directions between 90 and 350° at hub height.

There are several pronounced features: wind from the south-west sector was frequently associated with a wind speed between 5 and 15 m s^{-1}. This corresponds to the most frequent wind direction for the North Sea (Platis et al., 2018), and is typically associated with stable conditions in spring and summer (Schulz-Stellenfleth et al., 2022). Further, conditions with wind directions from the east were measured, which is also typically associated with stable conditions. Several flights were performed during relatively low wind speed from the north-west, when typically neutral or unstable atmospheric conditions are expected.

5.5 Humidity

Figure 10 shows the frequency of the occurrence of different values of relative humidity during all measurement flights. The profiles of relative humidity can be very different depending on atmospheric stability. On average, the relative humidity increases with altitude, which is caused by the decreasing temperature with altitude, as shown in Fig. 6. The decreasing relative humidity within the lowermost 100 m is in agreement with the increasing temperature in that altitude range.

6 Examples of measurements

In this section, a few impressions illustrate what can be done with the data. More and deeper applications with thorough scientific discussions are indicated as references.

6.1 Wind park wakes

Figure 4a shows an example of wakes downstream of several wind parks during Flight 12 in the afternoon on 29 June 2020, potentially superposed by spatial and temporal gradients of the wind speed. Despite the coverage with low-level stratocumulus clouds, the atmospheric conditions were stable, as the temperature of the air masses advected from land was higher than the water surface temperature of the North Sea. The main wind direction at hub height was 230° (south-west), and the mean wind speed was 15 m s^{-1}. The changes in the colour from red/orange to blue indicate a reduction in the wind speed to below 13 m s^{-1}. This can be observed north-east (downstream) of the wind park clusters N3 and N4. Further, the wind speed is reduced at the south-eastern edge of the flight pattern, which may be due to the proximity of the coast or downstream of the island of Heligoland. Wind park cluster N2 was partly not in operation on that day according to the flight protocol, which may explain that no pronounced reduction in wind speed is visible downstream.

6.2 Blockage effect

Figure 4b shows an example of measurements upstream of the wind park cluster N4 during flight 13 in the morning

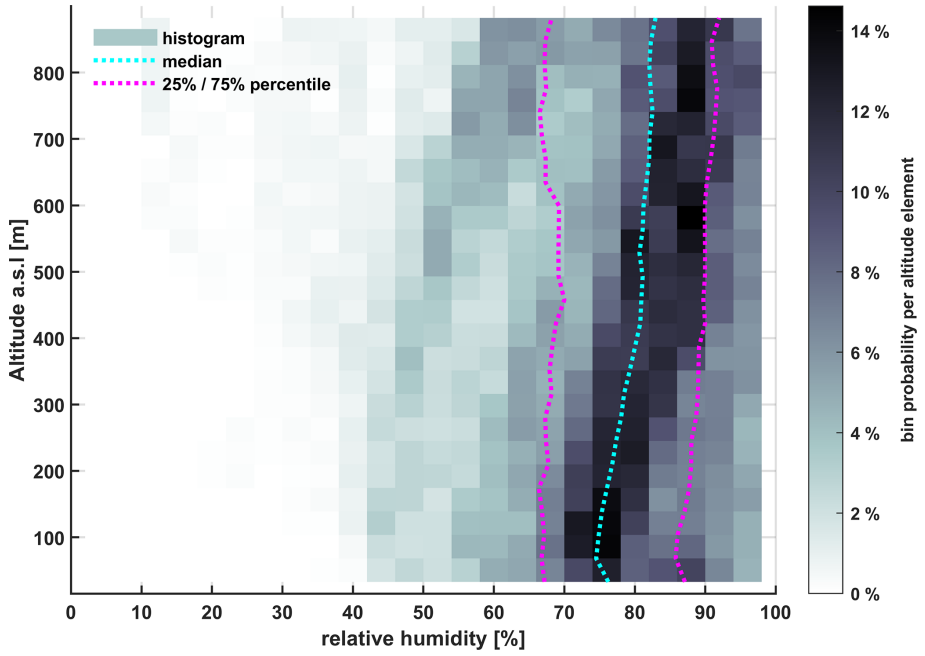

Figure 10. Relative humidity encountered during all measurement flights. The light-blue line represents the median of all profiles, the magenta lines indicate the percentiles including 25 % and 75 % of all values, and the grey scale is a histogram showing the probability of the occurrence of the relative humidity values.

on 30 June 2020. The main wind direction at hub height was 250° (west), and the mean wind speed was 17 m s^{-1}. A spatial and temporal gradient of the wind field is also obvious here, with higher wind speed toward the north and changes in wind speed between the individual flight legs, as can be seen by the different colours indicating a wind speed range between 13 m s^{-1} and 15 m s^{-1} in the southern part of the flight, where no influence of the blockage effect is expected. The variability in the wind speed for the time period of one flight leg (around 10 min) and for different flight legs is higher than the expected effect of wind speed reduction in the blockage effect in the range of a few percent. Therefore, continuously available datasets, e.g. from a scanning wind lidar, are more suitable to identify and quantify the blockage effect (Schneemann et al., 2021).

6.3 Coastal effect

Figure 5a illustrates the coastal effect, i.e. the spatial variability in the wind field close to and induced by the coast transition from higher to lower surface roughness and from higher surface temperature variability due to lower heat capacity to more constant surface temperatures due to the large heat capacity of the waterbody. At the edges of the individual legs, vertical profiles were performed to document the vertical distribution of wind, temperature and humidity, with enhanced wind speed for higher altitudes.

In this case, for wind from the south, the wind speed increases with the distance from the coast along the wind direction, the so-called fetch length. This is not only the more frequent case, but a systematic decrease in wind speed with distance from the coast is also possible, as described in Djath et al. (2022). Further, a high variability in the wind speed along the coast is observed as well. It may be influenced by local orography, with increased wind speed between the different islands and reduced wind speed downstream, as described in detail in Schulz-Stellenfleth et al. (2022).

6.4 Changes in the wind field above wind parks

Figure 5b illustrates the modification of the wind speed during a transect above the wind park N3 at a constant altitude of 250 m. The wind speed is enhanced at the edges of the wind park and reduced directly above. Similar investigations using airborne measurements above wind parks obtained during the project WIPAFF (Bärfuss et al., 2019; Lampert et al., 2020) are presented in Siedersleben et al. (2020) and Syed et al. (2023).

6.5 Effect of clouds on radiation

Figure 11 shows an example of the variation in the measured radiation with time when underpassing a cloud. As expected, the solar downward irradiance decreases under the cloud, which is visible here as the reduction from around 600 to 300 W m^{-2}. At the same time, the solar upward (reflected) irradiance decreases as well as less radiation reaches the surface. The terrestrial upward irradiance decreases slightly

(by less than $1\,W\,m^{-2}$) along the flight leg, probably due to, on average, slightly decreasing surface temperature (lowest panel of Fig. 11; see trend line) and independently of the cloud, as the water surface temperature does not rapidly change with cloud cover. The terrestrial downward irradiance increases slightly (around $1\,W\,m^{-2}$) due to the enhanced temperature of the cloud. The unfiltered raw data show spikes on the order of $< 0.5\,W\,m^{-2}$, but the causes have not been identified in more detail yet. Even if the sensor response time provided by the manufacturer is quite high and despite the hemispheric field of view of the sensors, suitable algorithms can help to estimate the cloud situation during the flights.

6.6 Sea surface temperature

Figure 12 shows measured sea surface temperatures in the area of the Jade stream close to the coast for several observation times within one day. For comparison, sea surface temperature values of the two relevant grid areas of the ERA5 model (Hersbach et al., 2018) are also shown in the diagrams. Depending on the tides and the exact location, the sea surface temperature varies around 2 °C during the same day. The agreement between ERA5 sea surface temperature and measured surface temperature was very close for the time of around 14:00 UTC. For other times of the day, the difference between ERA5 sea surface temperature and the measured temperature was in the range of 1 °C. This indicates that the ERA5 model is not capable of resolving the temporal changes in sea surface temperature associated with tides very well. The gathered data have the potential to deliver contributions for a better understanding of the complex stream and surface temperature situation in coastal areas.

7 Data availability

The data are available on PANGAEA at https://doi.org/10.1594/PANGAEA.955382 (Rausch et al., 2023a). Besides the abovementioned data on temperatures, humidity, wind, sea surface and radiation, the dataset contains aircraft position, GPS altitude (WGS84 coordinate system), radar altimeter distance to ground, aircraft velocity (ground speed in north/east/down components),ž and aircraft attitude. ERA5 reanalysis data are available at https://doi.org/10.24381/cds.adbb2d47 (Hersbach et al., 2018).

8 Conclusions

The X-Wakes flights over the North Sea in 2020/2021 expand the measurements performed during the airborne measurement campaign WIPAFF (Bärfuss et al., 2019; Lampert et al., 2020) in 2016/2017. They serve to investigate the decay of wind park wakes at hub height in the far field. New aspects are

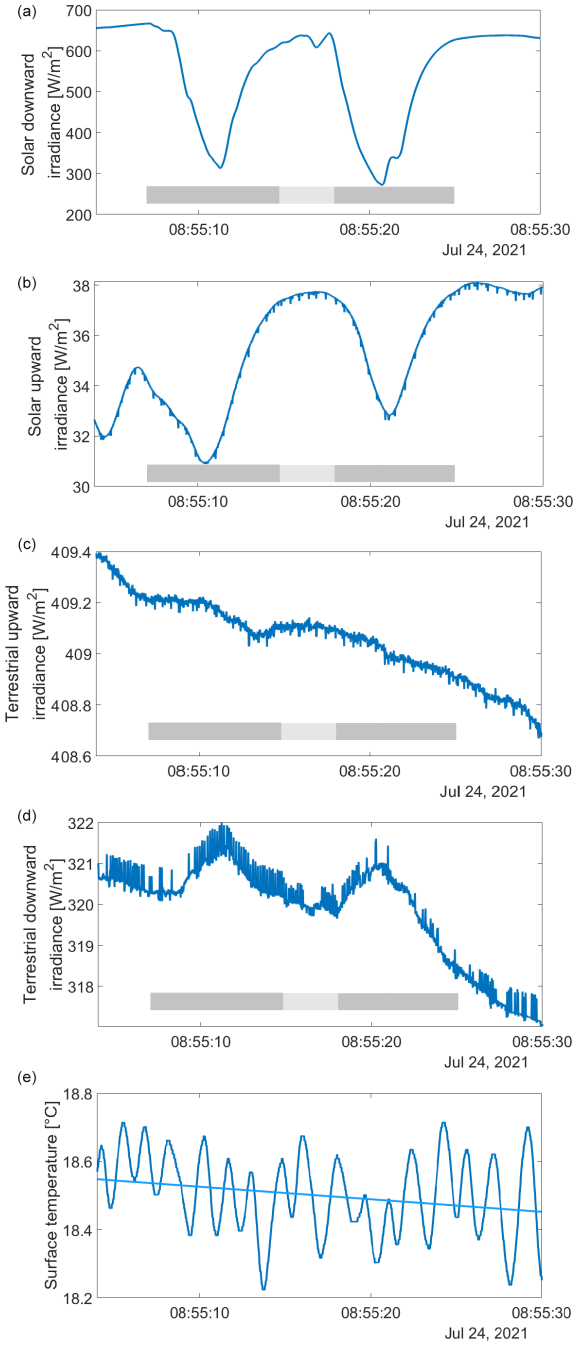

Figure 11. Example of the variation in time of the measured irradiance and surface temperature when underpassing a cloud. **(a–e)** Solar downward irradiance, solar upward (reflected) irradiance, terrestrial upward (emitted) irradiance, terrestrial downward irradiance and surface temperature. The grey bar shows the approximate cloud position. The time series of surface temperature includes a trend line.

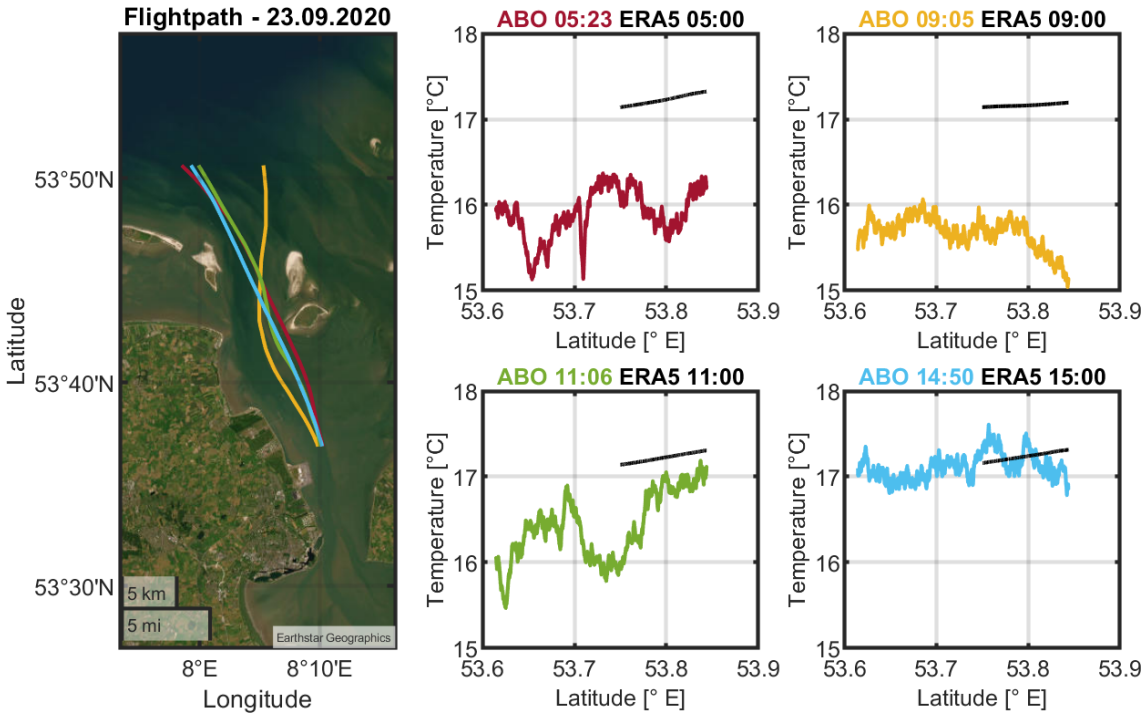

Figure 12. Example of sea surface temperature measurements near the coast compared to the two closest points of reanalyses of the ERA5 model for different overpass times; ABO refers to aircraft-based observation, and times are provided in UTC.

- more wind parks in operation;
- new flight patterns, blocking and coast;
- flights also during unstable conditions;
- some flights with simultaneous observations of two aircraft to separate temporal and spatial variability;
- new radiation sensor package on second aircraft.

The measurements were embedded in continuous observational programmes like the FINO1 meteorological mast and dedicated wind lidar campaigns, some of which are publicly available as well (Rausch et al., 2023b).

The data have already been used for several investigations within the project X-Wakes, which are referenced in the respective section.

Supplement. A short video with impressions from the research flights is available in the Supplement for illustration purposes. The supplement related to this article is available online at: https://doi.org/10.5194/essd-16-4777-2024-supplement.

Author contributions. The authors all contributed directly to creating the data base by performing the measurement flights. AL, RH, TF, KB and TR designed the flight strategy. RH, TF, MC and MA piloted the aircraft. AL, KB, MB, JF and TR were responsible for the data acquisition. UB, JF, MB and MC developed the data acquisition for the new aircraft. HS and MB were responsible for airworthiness certification of the sensors and maintenance of the sensors. The manuscript was initiated and drafted by AL. The figures of the measurement data were provided by KB. All authors contributed to the writing and editing of the manuscript.

Competing interests. The contact author has declared that none of the authors has any competing interests.

Disclaimer. Publisher's note: Copernicus Publications remains neutral with regard to jurisdictional claims made in the text, published maps, institutional affiliations, or any other geographical representation in this paper. While Copernicus Publications makes every effort to include appropriate place names, the final responsibility lies with the authors.

Acknowledgements. The authors would like to thank the partners of the project for the collaboration and in particular for the fruitful discussions on the preparation of the campaign and the measurement data. The authors would like to thank Johannes Hammel and all other students involved in the analysis of the data.

Financial support. The project X-Wakes was funded by the German Federal Ministry of Economic Affairs and Energy (BMWi),

now the Federal Ministry for Economic Affairs and Climate Action (BMWK), under grant no. 03EE3008B on the basis of a decision by the German Bundestag.

This open-access publication was funded by Technische Universität Braunschweig.

Review statement. This paper was edited by Tobias Gerken and reviewed by Tobias Gerken and one anonymous referee.

References

Akhtar, N., Geyer, B., Rockel, B., Sommer, P. S., and Schrum, C.: Accelerating deployment of offshore wind energy alter wind climate and reduce future power generation potentials, Nat. Sci. Rep., 11, 11826, https://doi.org/10.1038/s41598-021-91283-3, 2021.

Angelou, N., Mann, J., and Dubreuil-Boisclair, C.: Revealing inflow and wake conditions of a 6 MW floating turbine, Wind Energ. Sci., 8, 1511–1531, https://doi.org/10.5194/wes-8-1511-2023, 2023.

Bärfuss, K., Pätzold, F., Altstädter, B., Kathe, E., Nowak, S., Bretschneider, L., Bestmann, U., and Lampert, A.: New Setup of the UAS ALADINA for Measuring Boundary Layer Properties, Atmospheric Particles and Solar Radiation, Atmosphere, 9, 28, https://doi.org/10.3390/atmos9010028, 2018.

Bärfuss, K., Hankers, R., Bitter, M., Feuerle, T., Schulz, H., Rausch, T., Platis, A., Bange, J., and Lampert, A.: In-situ airborne measurements of atmospheric and sea surface parameters related to offshore wind parks in the German Bight, PANGAEA [data set], https://doi.org/10.1594/PANGAEA.902845, 2019.

Bärfuss, K., Djath, B., Lampert, A., and Schulz-Stellenfleth, J.: Airborne LiDAR Measurements of the sea surface properties in the German Bight, IEEE T. Geosci. Remote, 59, 4608–4617, https://doi.org/10.1109/TGRS.2020.3017861, 2020.

Bärfuss, K., Schulz-Stellenfleth, J., and Lampert, A.: The Impact of Offshore Wind Farms on Sea State Demonstrated by Airborne LiDAR Measurements, J. Mar. Sci. Eng., 9, 644, https://doi.org/10.3390/jmse9060644, 2021.

Broström, G.: On the influence of large wind farms on the upper ocean circulation, J. Marine Syst., 74, 585–591, 2008.

Cañadillas, B., Foreman, R., Barth, V., Siedersleben, S., Lampert, A., Platis, A., Djath, B., Schulz-Stellenfleth, J., Bange, J., Emeis, S., and Neumann, T.: Offshore wind farm wake recovery: Airborne measurements and its representation in engineering models, Wind Energy, 23, 1249–1265, https://doi.org/10.1002/we.2484, 2020.

Cañadillas, B., Beckenbauer, M., Trujillo, J. J., Dörenkämper, M., Foreman, R., Neumann, T., and Lampert, A.: Offshore wind farm cluster wakes as observed by long-range-scanning wind lidar measurements and mesoscale modeling, Wind Energ. Sci., 7, 1241–1262, https://doi.org/10.5194/wes-7-1241-2022, 2022.

Canadillas, B., Wang, S., Ahlert, Y., Djath, B., Barekzai, M., Foreman, R., and Lampert, A.: Coastal horizontal wind speed gradients in the North Sea based on observations and ERA5 reanalysis data, Meteorol. Z., 32, 207–228, https://doi.org/10.1127/metz/2022/1166, 2023.

Christiansen, M. B. and Hasager, C. B.: Wake effects of large offshore wind farms identified from satellite SAR, Remote Sens. Environ., 98, 251–268, 2005.

Corsmeier, U., Hankers, R., and Wieser, A.: Airborne turbulence measurements in the lower troposphere onboard the research aircraft Dornier 128-6, D-IBUF, Meteorol. Z., 10, 315–329, 2001.

Djath, B., Schulz-Stellenfleth, J., and Cañadillas, B.: Study of Coastal Effects Relevant for Offshore Wind Energy Using Spaceborne Synthetic Aperture Radar (SAR), Remote Sens., 14, 1688, https://doi.org/10.3390/rs14071688, 2022.

El-Asha, S., Zhan, L., and Lungo, G.V.: Quantification of power losses due to wind turbine wake interactions through SCADA meteorological and wind LiDAR data, Wind Energy, 20, 1823–1839, 2017.

Fast, J. D., Berg, L. K., Alexander, L., Bell, D., D'Ambro, E., Hubbe, J., Kuang, C., Liu, J., Long, C., Matthews, A., Mei, F., Newsom, R., Pekour, M., Pinterich, T., Schmid, B., Schobesberger, S., Shilling, J., Smith, J. N., Springston, S., Suski, K., Thornton, J. A., Tomlinson, J., Wang, J., Xiao, H., and Zelenyuk, A.: Overview of the HI-SCALE Field Campaign: A New Perspective on Shallow Convective Clouds, B. Am. Meteorol. Soc., 100, 821–840, https://doi.org/10.1175/BAMS-D-18-0030.1, 2019.

Fischereit, J., Larsen, X. G., and Hahmann, A. N.: Climatic Impacts of Wind-Wave-Wake Interactions in Offshore Wind Farms, Front. Energy Res., 10, 881459, https://doi.org/10.3389/fenrg.2022.881459, 2022.

Hersbach, H., Bell, B., Berrisford, P., Biavati, G., Horányi, A., Muñoz Sabater, J., Nicolas, J., Peubey, C., Radu, R., Rozum, I., Schepers, D., Simmons, A., Soci, C., Dee, D., and Thépaut, J.-N.: ERA5 hourly data on single levels from 1959 to present, Copernicus Climate Change Service (C3S) Climate Data Store [data set], https://doi.org/10.24381/cds.adbb2d47, 2018.

Lampert, A., Bärfuss, K., Platis, A., Siedersleben, S., Djath, B., Cañadillas, B., Hunger, R., Hankers, R., Bitter, M., Feuerle, T., Schulz, H., Rausch, T., Angermann, M., Schwithal, A., Bange, J., Schulz-Stellenfleth, J., Neumann, T., and Emeis, S.: In situ airborne measurements of atmospheric and sea surface parameters related to offshore wind parks in the German Bight, Earth Syst. Sci. Data, 12, 935–946, https://doi.org/10.5194/essd-12-935-2020, 2020.

Lenschow, D. H.: The Measurement of Air Velocity and Temperature Using the NCAR Buffalo Aircraft Measuring System; National Center for Atmospheric Research, Boulder, CO, NCARTN/EDD-74, 39 pp., https://doi.org/10.5065/D6C8277W, 1972.

Li, X., and Lehner, S.: Observation of TerraSAR-X for studies on offshore wind turbine wake in near and far fields, IEEE J. Sel. Top. Appl. Earth Obs., 6, 1757–1768, 2013.

Lundquist, J., DuVivier, K. K., Kaffine, D., and Tomaszewski, J. M.: Costs and consequences of wind turbine wake effects arising from uncoordinated wind energy development, Nature Energy, 4, 26–34, 2019.

Manzano-Agugliaro, F., Sanchez-Calero, M., Alcayde, A., San-Antonio-Gomez, C., Pereo-Moreno, A.-J., and Salmeron-Manzano, E.: Wind Turbine Offshore Foundations and Connections to Grid, Inventions 2020, 5, 1, 8, 2020.

Nygaard, N. G. and Hansen, S. D.: Wake effects between two neighbouring wind farms, J. Phys. Conf. Ser., 753, 032020, https://doi.org/10.1088/1742-6596/753/3/032020, 2016.

Pettas, V., Kretschmer, M., Clifton, A., and Cheng, P. W.: On the effects of inter-farm interactions at the offshore wind farm Alpha Ventus, Wind Energ. Sci., 6, 1455–1472, https://doi.org/10.5194/wes-6-1455-2021, 2021.

Paskyabi, M. B.: Offshore Wind Farm Wake Effect on Stratification and Coastal Upwelling, Energy Proced., 80, 131–140, 2015.

Platis, A., Siedersleben, S., Bange, J., Lampert, A., Bärfuss, K., Hankers, R., Cañadillas, B., Foreman, R., Schulz-Stellenfleth, J., Djath, B., Neumann, T., and Emeis, S.: First in situ evidence of wakes in the far field behind offshore wind farms, Sci. Rep., 8, 2163, https://doi.org/10.1038/s41598-018-20389-y, 2018.

Platis, A., Bange, J., Bärfuss, K., Cañadillas, B., Hundhausen, M., Djath, B., Lampert, A., Schulz-Stellenfleth, J., Siedersleben, S., Neumann, T., and Emeis, S.: Long-range modifications of the wind field by offshore wind parks – results of the project WIPAFF, Meteorol. Z., 29, 355–376, https://doi.org/10.1127/metz/2020/1023, 2020.

Platis, A., Hundhausen, M., Lampert, A., Emeis, S., and Bange, J.: The Role of Atmospheric Stability and Turbulence in Offshore Wind-Farm Wakes in the German Bight, Bound.-Lay. Meteorol., 182, 441–469, https://doi.org/10.1007/s10546-021-00668-4, 2022.

Platis, A., Büchau, Y., Zuluaga, S., and Bange, J.: The impact of offshore wind farms on the latent heat flux, Meteorol. Z., 32, 4, 261–277, https://doi.org/10.1127/metz/2023/1171, 2023.

Ponce de León, S., Bettencourt, J. H., and Kjerstad, N.: Simulation of Irregular Waves in an Offshore Wind Farm with a Spectral Wave Model, Cont. Shelf Res., 31, 1541–1557, 2011.

Rausch, T., Bärfuss, K., Hankers, R., Bitter, M., Feuerle, T., Cremer, M., Angermann, M., Füllgraf, J., and Lampert, A.: In-situ airborne measurements of atmospheric and sea surface parameters related to offshore wind parks in the German Bight, PANGAEA [data set], https://doi.org/10.1594/PANGAEA.955382, 2023a.

Rausch, T., Cañadillas, B., and Lampert, A.: Coastal vertical wind lidar measurements of horizontal wind speed and wind direction from 40 to 500 m at Norderney island, German Bight, North Sea, Germany, PANGAEA [data set], https://doi.org/10.1594/PANGAEA.953770, 2023.

Rivier, S., Bennis, A.-C., Pinon, G., Magar, V., and Gross, M.: Parameterization of wind turbine impacts on hydrodynamics and sediment transport, Ocean Dynam., 66, 1285–1299, 2016.

Schneemann, J., Rott, A., Dörenkämper, M., Steinfeld, G., and Kühn, M.: Cluster wakes impact on a far-distant offshore wind farm's power, Wind Energ. Sci., 5, 29–49, https://doi.org/10.5194/wes-5-29-2020, 2020.

Schneemann, J., Theuer, F., Rott, A., Dörenkämper, M., and Kühn, M.: Offshore wind farm global blockage measured with scanning lidar, Wind Energ. Sci., 6, 521–538, https://doi.org/10.5194/wes-6-521-2021, 2021.

Schulz-Stellenfleth, J., Emeis, S., Dörenkämper, M., Bange, J., Cañadillas, B., Neumann, T., Schneemann, J., Weber, I., zum Berge, K., Platis, A., Djath, B., Gottschall, J., Vollmer, L., Rausch, T., Barekzai, M., Hammel, J., Steinfeld, G., and Lampert, A.: Coastal impact on offshore wind farms – a review focusing on the German Bight area, Meteorol. Z., 31, 289–315, https://doi.org/10.1127/metz/2022/1109, 2022.

Siedersleben, S. K., Lundquist, J. K., Platis, A., Bange, J., Bärfuss, K., Lampert, A., Cañadillas, B., Neumann, T., and Emeis, B.: Micrometeorological impacts of offshore wind farm as seen in observations and simulations, Environ. Res. Lett., 13, 124012, https://doi.org/10.1088/1748-9326/aaea0b, 2018a.

Siedersleben, S. K., Platis, A., Lundquist, J. K., Lampert, A., Bärfuss, K., Cañadillas, B., Djath, B., Schulz-Stellenfleth, J., Neumann, T., Bange, J., and Emeis, S.: Evaluation of a Wind Farm Parametrization for Mesoscale Atmospheric Flow Models with Aircraft Measurements, Meteorol. Z. [preprint], https://doi.org/10.1127/metz/2018/0900, 2018b.

Siedersleben, S. K., Platis, A., Lundquist, J. K., Djath, B., Lampert, A., Bärfuss, K., Cañadillas, B., Schulz-Stellenfleth, J., Bange, J., Neumann, T., and Emeis, S.: Turbulent kinetic energy over large offshore wind farms observed and simulated by the mesoscale model WRF (3.8.1), Geosci. Model Dev., 13, 249–268, https://doi.org/10.5194/gmd-13-249-2020, 2020.

Spyridonidou, S. and Vagiona, D. G.: Systematic Review of Site-Selection Processes in Onshore and Offshore Wind Energy Research, Energies, 13, 5906, https://doi.org/10.3390/en13225906, 2020.

Stickney, T. M., Shedlov, M. W., and Thompson, D. I.: Goodrich Total Temperature Sensors, Technical Report, 5755, 32 pp., https://www.flightdatacommunity.com/wp-content/uploads/downloads/2013/02/TAT-Report.pdf (last access: 18 April 2022), 1994.

Syed, A. H., Mann, J., Platis, A., and Bange, J.: Turbulence structures and entrainment length scales in large offshore wind farms, Wind Energ. Sci., 8, 125–139, https://doi.org/10.5194/wes-8-125-2023, 2023.

Veers, P., Dykes, K., Lantz, E., Barth, S., Bottasso, S. B., Carlson, O., Clifton, A., Green, J., Holttinen, H., Laird, D., Lehtomäki, V., Lundquist, J. K., Manwell, J., Marquis, M., Meneveau, C., Moriarty, P., Munduate, X., Muskulus, M., Naughton, J., Pao, L., Paquette, J., Peinke, J., Robertson, A., Sanz Rodrigo, J., Sempreviva, A.M., Smith, J.C., Tuohy, A., and Wiser, R.: Grand challenges in the science of wind energy, Science, 366, 443, https://doi.org/10.1126/science.aau2027, 2019.

Wiser, R., Rand, J., Seel, J., Beiter, P., Baker, E., Lantz, E., and Gilman, P.: Expert elicitation survey predicts 37 % to 49 % declines in wind energy costs by 2050, Nature Energy, 6, 5555–565, 2021.

zum Berge, K., Centurelli, G., Dörenkämper, M., Bange, J., and Platis, A.: Evaluation of Engineering Models for Large-Scale Cluster Wakes With the Help of In Situ Airborne Measurements, Wind Energy, 27, 1040–1062, https://doi.org/10.1002/we.2942, 2024.